

Experimental approach for the determination of the Bridgman's necking parameters

Philip Siegmann, Cristina Alén-Cordero  and Rocío Sánchez-Montero

Department of Signal Theory and Communications, Escuela Politécnica Superior, University of Alcalá, Alcalá de Henares, 28805, Spain

E-mail: philip.siegmann@uah.es, cristina.alen@uah.es and rocio.sanchez@uah.es

Received 14 March 2019, revised 29 May 2019

Accepted for publication 17 June 2019


Published 6 September 2019



Abstract

Two ways of determining Bridgman's parameters are presented to estimate the equivalent Bridgman stress–strain (BSS) curve after the onset of necking in cylindrical specimens. The accurate experimental determination of the minimum necking radius, r_N , and the radius of curvature of the necking, R_N , are considered to be the main problems in applying Bridgman's model to obtain the equivalent BSS curve and describe the plastic behaviour of materials. Using the combined technique of 2D digital image correlation and fringe projection, the 3D positions and displacements of the surface elements are determined for each load stage of a tensile test on steel, aluminium (Al) and copper (Cu) bars. The axial displacements are well fitted with an empirical function that allows accurate estimation of the beginning of necking and its location on the specimen. From the 3D positions, both Bridgman's parameters are estimated by adjusting a torus to the necking zone. The 3D measurements around the necking position have to be well defined to obtain the parameters in a feasible way, because the real necking profile does not fit well with the half-circle proposed by Bridgman. Nonetheless, the estimated r_N parameters are noisy, affecting the BSS curve. Therefore, an alternative and simpler way for estimating r_N and R_N is also proposed, only requiring the measurement of total axial displacements along the loading axis of each surface element. In this way, the BSS curve obtained is smooth, although it somewhat underestimates the same curve obtained using experimentally measured 3D data.

Keywords: true stress–strain curve, digital image correlation, fringe projection, onset of necking, Bridgman's model

 Supplementary material for this article is available [online](#)

(Some figures may appear in colour only in the online journal)

1. Introduction

In terms of structural design, only the elastic behaviour of materials is usually considered, thus the engineering stress–strain curve (ESS, S - e) obtained in a tensile test can be used to characterize the behaviour of material. The ESS curve takes into account the stress applied to the specimen as the applied force divided by the initial cross-section. It is therefore lower than the actual stress required for the deformation, because

the cross-section reduction is not considered. Thus, ESS overestimates the stress for which the material will suffer plastic deformation. However, either for designs in which weight is an important factor or for predicting the behaviour of structures that are overloaded and produce deformations that go further the elastic range, a more realistic analysis of stress–strain curve is required [1]. Moreover, for on-going monitoring of the performance of machines or structures under working conditions, or to predict deformation and the ductile

fracture propagation of material a sound approach to estimate the behaviour of the material beyond the elastic range is essential [2].

There are two different approaches to cover behaviour of material in the non-elastic range: the true stress–strain (TSS) curve and the Hollomon’s law or reference stress strain curve (RSS).

The TSS curve ($\sigma - \varepsilon$) can be obtained from the force–elongation measurements ($F - \delta$) of a tensile test as follows:

$$\begin{aligned}\sigma &= (F/A_0) (1 + \delta/H_0) \\ \varepsilon &= \ln(1 + \delta/H_0),\end{aligned}\quad (1)$$

where A_0 and H_0 are the initial cross section and length of the specimen, respectively.

The TSS takes into account the cross-section reduction of the specimen while it is increasingly loaded, considering that the cross-section reduction is uniform along the specimen’s length. This approach is therefore not valid for materials that present plastic deformation, in particular when deformation starts to concentrate around a necking zone. At this point, the state of stresses at the necking zone changes from uniaxial to triaxial [3].

Hollomon’s law (RSS) is also generally accepted to describe the behaviour of material in the case of uniform plastic deformation. Some authors have termed it also as the equivalent TSS curve and formulated it as follows:

$$\sigma_{\text{equ}}(\varepsilon_{\text{equ}}) = k \cdot \varepsilon_{\text{equ}}^n, \quad (2)$$

where k denotes the strength coefficient and ε_N stands for the strain hardening exponent defined as the true strain value at the onset of necking. Values of these parameters are obtained as explained in [3].

After the onset of necking, Bridgman’s analytical model is the most widely accepted for describing the TSS curve [3–7] in cylindrical specimens. This approach is based on the experimental determination of the Bridgman coefficient, C , to obtain the equivalent stress–strain curve in post-necking phase, when non-uniform plastic deformation occurs. The formulation is as follows:

$$\sigma_{\text{equ}} = C \cdot (\sigma_a)_{\text{av}}, \quad (3)$$

where $(\sigma_a)_{\text{av}} = F/A$ is the axial average stress at the instantaneous smallest cross section (A).

Bridgman’s model approaches the geometrical shape of the necking with the inner surface of a torus, whose revolution axis coincides with the tensile axis of the cylindrical specimen. The torus radius is the curvature radius of the necking R_N and, the radius of the smallest cross section of the necking, r_N is related to the radius of revolution of the torus with $(R_N + r_N)$. With these two geometrical parameters, the Bridgman’s coefficient is obtained as follows:

$$C = \left[\left(1 + \frac{2R_N}{r_N} \right) \cdot \ln \left(1 + \frac{r_N}{2R_N} \right) \right]^{-1}. \quad (4)$$

Equation (4) requires the determination of R_N and r_N , for each load stage after the onset of necking and at the exact location of the necking point. This has been proven to be the main problem when applying the Bridgman’s model.

Several research methodologies have been studied to define the stress–strain relation, in non-uniform plastic deformation phase. Some of them use finite element (FE) simulations to obtain the TSS curve by comparing simulation outputs with the measurements obtained from a tensile test. In [3], a weighted-average correction method was proposed for FE simulation of a tensile test of a rod specimen after necking. In [5], a stress correction parameter obtained by applying a linear regression model to the test results, was introduced for the stress–strain curve of plane specimens; it was then verified using iterative parametric FE simulations. In [7], the Bridgman’s stress–strain curve was calculated using the radii and necking curvature from the acquired images of different steel specimens subjected to tensile tests. The obtained curve was used as input for FE simulations of tensile tests. Other studies [8, 9] propose the use of a rigid plastic FE method for simulation of tensile tests and to predict the strain hardening behaviour of the material and the mechanism of the necking formation.

A different approach to estimating post-necking behaviour and sidestepping the difficulty in experimentally obtaining the Bridgman’s parameters are based on different mathematical formulations of the stress–strain curves [10, 11]. In [10], a mathematical model for predicting the cylindrical specimen’s deformation is proposed and compared with FE analysis results, but without experimental validation. In [11], mathematical regression equations are used to fit the experimental stress–strain curves of stainless steel specimens; however, necking formation is disregarded but instead, a uniform elongation. In [12], the axial strain component of the necking zone of a cylindrical specimen, is obtained from images of the specimen’s surface marked with regularly distributed dots. The specimen’s profile is also obtained by selecting certain points along the specimen’s contour and fitting them to a quadratic function. From that, the other two strain components are obtained using a specially developed mathematical model. Validation is then performed using numerical simulation with the *Abacus* software. Nonetheless, this edge tracing procedure for selecting the data points does not provide a robust procedure to determine the necking curvature from the selected profile. As will be addressed later on, it strongly depends on the range of data points around the necking zone used to fit the necking curvature.

Precise experimental measurements of large displacement maps for entire specimen surfaces can be obtained with a digital image correlation (DIC) technique [13]. It can be performed with one camera (2D-DIC) or with two cameras (3D-DIC). In [14–16], DIC was used to study deformation in the plastic range of different materials. In [17], 3D-DIC was used to obtain TSS curves at two sections of the specimen, near and far from the fracture location, and the evolution of the plastic zone was analysed, by mapping the measured displacements during the experimental tensile test. Furthermore, the stress–strain curves obtained experimentally with DIC can be used to validate FE models used to simulate material plastic behaviour. In this sense, several studies combine numerical simulations (FEM) and DIC, on plane specimens made of copper [18], hourglass type specimens of carbon steel [19],

cylindrical specimens of different aluminium alloys [20] or even titanium [21]. In [22], 3D-DIC is used to obtain the full reconstruction of the necking area in different specimens (flat and cylindrical) at high speed.

When applying the Bridgman's method for rod specimens [3, 5, 7, 10], it is essential to set up an accurate and reproducible procedure to obtain the geometrical parameters of the necking (r_N and R_N) along the whole test and thus, attain a more accurate approximation of post-necking equivalent stress–strain curve. As mentioned before, the use of 3D-DIC has proved to be a valuable tool for determining the Bridgman parameters [20]. However, on one hand, the procedure of obtaining these parameters from experimental 3D data has not yet been proposed in a feasible way. It would be necessary to specify which data points from the necking zone have to be used to determine R_N . On the other hand, the main inconvenient of the 3D-DIC is the complex image-processing algorithms that it requires, which makes it difficult to create the required self-made software. In addition, the commercially available ones are quite expensive and are not always affordable; therefore, an alternative and more accessible technique would be of interest.

In the present work, a self-made full-field technique combining 2D-DIC and fringe projection (FP), (FP + 2D-DIC) is used to obtain the 3D displacement maps of the surface of cylindrical specimens subjected to a tensile test. The 2D-DIC makes possible to measure the in-plane displacements of the surface elements in x - and y -direction and, FP uses an additional fringe projector to measure the out-of-plane (z -displacements) [23–25]. The obtained axial displacement (AD) profiles and the 3D shape around the necking zone are then used to localize and determine the necking parameters at each load stage in a well-established and reproducible way. This method also allows finding an empirical axial displacement equation, for estimating each surface element of our cylindrical specimens at the necking zone. However, the experimentally obtained values for r_N and R_N are somewhat noisy and the noise in r_N critically affects the average axial stress at the smallest cross section. To prevent it, from the empirical axial displacement equation, an analytical model is derived for the radii of the specimen along the loading axis, from which both the smallest necking radius and the necking curvature can be obtained in an alternative way. This delivers noise-free values for both r_N and R_N , so the equivalent stress–equivalent strain curve is obtained in a feasible way.

The remainder of the paper is organized as follows: the experimental set up of the tensile test with the combined FP + 2D-DIC system and the retrieved data are outlined in Section 2 for three different specimens (although up to three specimens of each material were tested giving practically the same results). The detailed description of the image processing performed after obtaining the in- and out-of-plane displacements of the 2D-DIC and FP results are then presented in section 3. The image processing performed by 2D-DIC and FP are not described in detail since they are already commonly used and well-known techniques. The two proposed procedures for the feasible determination of Bridgman parameters are given in section 4. The results of the estimated

Bridgman parameters, the average axial stress at the smallest cross section and the equivalent stress–strain curve according to Bridgman are shown in section 5. The final section is dedicated to the discussion of the results obtained and to give some ending conclusions and remarks on the work carried out.

2. Experimental set-up of the tensile test

2.1. Tensile test

The tensile tests were performed on normalized cylindrical specimens of steel, aluminium and copper of 6 mm diameter and with a gage length of $H_0 = 30$ mm each.

To perform the tensile test, the WP300 test bench (GÜNT) equipped with electronic force and a displacement measurement instruments was used, in addition to data acquisition equipment (WP300.20), to obtain values of force and the corresponding displacement with a precision of 0.5 kN and 0.01 mm, respectively. The 2D-DIC + FP system consists of a colour camera and a colour projector. The camera visualizing the specimen must be placed perpendicular to the specimen's cylindrical axis (x -axis) and the projector projects fringes perpendicular to this axis, but with a certain incidence angle, as shown in figure 1. Both the camera and the projector are joined together and fixed on a mobile platform, allowing the movement of both elements towards and away from the specimen to aligning and calibrate the system. The whole 2D-DIC + FP system is mounted on a tripod, which enables the correct configuration and alignment of the set-up. The detailed alignment and calibration procedures have previously been described in [24, 25]. Furthermore, the specimen needs to be painted with red speckles on a white background and the fringes must alternate in white and blue. Then, from each red–green–blue (RGB) image acquired by the camera, it is possible to separate the fringe information from the speckle information by simply using the R channel or the B channel respectively, as will be shown later. The speckle images are used to compute the in-plane displacements (in the x - and y -directions) for each surface element (i.e. the surface that is visualized by one pixel) of the specimen, these being displacements on a plane perpendicular to the camera's optical axis. The fringe images are then used to compute the out-of-plane displacements (in the z -direction) for each surface element or the 3D shape.

The test was then performed manually by increasing the load applied on the specimen at a constant speed of about 0.5 mm specimen elongation per minute. Two separate measurements were taken at the same time:

- i. Loads and displacements data sets ($F - \delta$) acquired with the WP 300.20 GÜNT system. Size of the data set was between 171 for steel, 148 for copper and 64 for Al.
- ii. Images acquired with the FP + 2D-DIC system and corresponding loads (from which the axial displacements were obtained after image processing).

The number of acquired images ($S = 56$ for steel, $S = 23$ for copper and $S = 18$ for aluminium), was lower than the number of ($F - \delta$) pairs acquired by the GÜNT system.

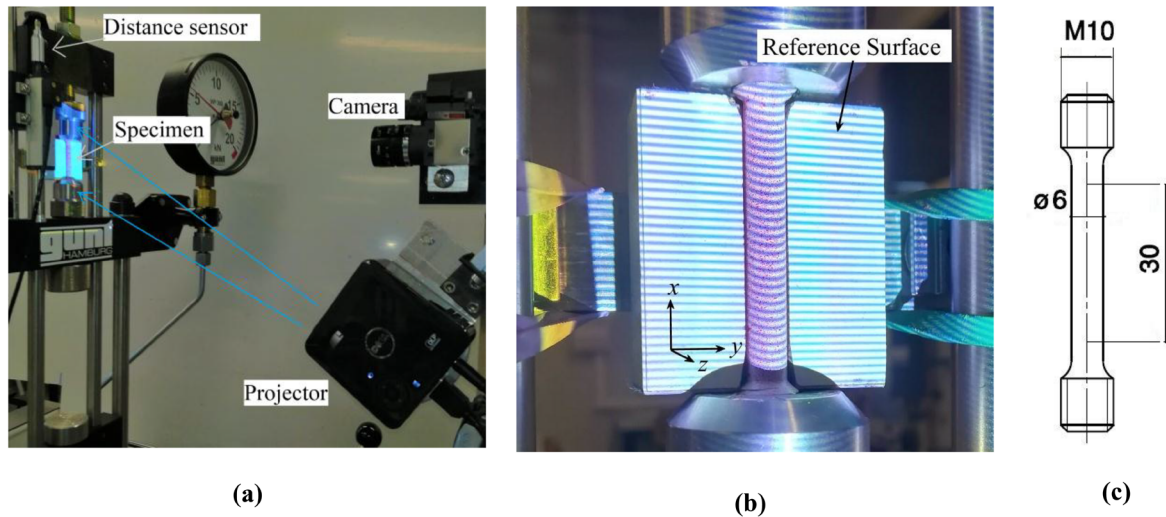


Figure 1. (a) Experimental set-up; (b) test specimen painted with red speckles on white background and illuminated with blue white fringes; (c) schematic of tensile specimen in mm.

A good correspondence between the two sets of data (axial displacements acquired with GÜNT acquisition system and those obtained from 2D-DIC) was found through the elongation measurements. In particular, both identified the same ultimate strength position. Thus, the force for each captured image could be assigned.

2.2. Experimental tensile test results

As shown in figure 2, the tensile test measurements ($F - \delta$) of the three samples were obtained with the GÜNT and FP + 2D-DIC systems at the same time, but with a different sampling interval.

The images at the different loading stages acquired with FP + 2D-DIC are indicated with squares, triangles and diamonds respectively for specimens 1, 2 and 3. The continuous line indicates the almost continuous data points acquired with the GÜNT system. The determination of the elongation values from the FP + 2D-DIC system are explained in the next section. The onset of necking is also indicated according to Considère's criterion [9], such that the slope of the force elongation curve becomes zero; this corresponds to the point of ultimate stress (corresponding to the maximum load) of the ESS curve, when the true strain reaches the strain-hardening exponent, ϵ_N .

Figure 3 shows the corresponding TSS curve (equation (1)) and the RSS curve (equation (2)) of the three samples. The RSS curve is generally considered applicable after the elastic range until the onset of necking, as shown in figure 3, where this point is marked with respective crosses. The first specimen (steel) experienced ductile fracture at a total axial elongation of 5.08 mm. Onset of necking appeared, according to Considère's criterion, at $\delta = 1.6$ mm and $F = 14.65$ kN, which corresponds to an engineering stress of $S_e = 488.4$ MPa and an engineering strain of $e = 5.65\%$.

The strength coefficient and the strain hardening exponent for the RSS curve (equation (2)) were $k = 605.19$ MPa and $\epsilon_N = 0.05497$. As will be shown in the following sections,

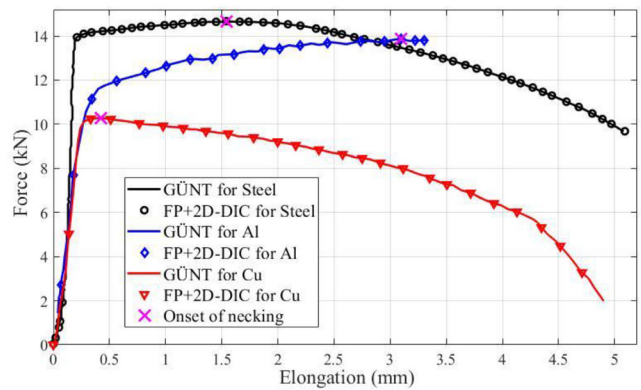


Figure 2. Force-displacement curves obtained at the tensile test for all specimens, with GÜNT and with FP + 2D DIC.

data processed from FP + 2D-DIC give the onset of necking for the steel sample at the load stage $s = 22$, corresponding to an axial elongation of 1.65 mm, which is in good agreement with Considère's criterion (a second specimen of steel was tested in the same way and the results were practically the same and are therefore not shown here).

The next specimen was an aluminium rod bar (specimen 2). It underwent a total axial elongation of 3.3 mm, at which point fracture occurred. The onset of necking appeared at an engineering stress of $S_e = 462$ MPa and an engineering strain of $e = 10.9\%$, produced at a force of $F = 13.86$ kN; the axial displacement registered during the test was about 3.1 mm. The strength coefficient and the strain-hardening exponent necessary to determine the RSS curve were respectively $k = 648$ MPa and $\epsilon_N = 0.1040$.

This specimen presented a fragile rupture, and no necking formation was detected with the FP + 2D-DIC data analysis. Considère's criterion placed the onset of necking at about 0.2 mm before the fracture, but there was an error of about the same value at this position associated with the noise at the maximum force in the last steps of the acquired GÜNT data. Therefore, it can be considered that no necking formation

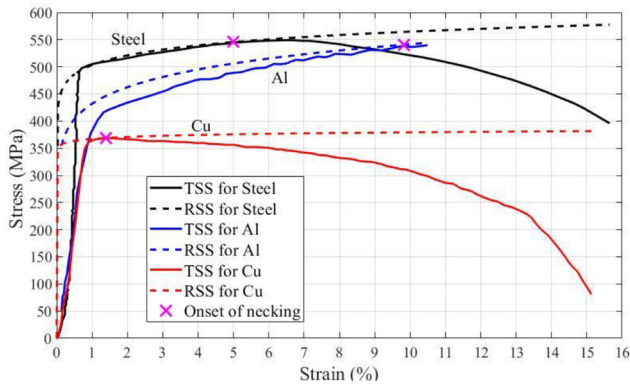


Figure 3. TSS and RSS curves and onset of necking according to Considère's criterion for all specimens.

happened in the case of this specimen. For this, the RSS is not appropriate for describing the material behaviour.

The last specimen was a copper rod bar (specimen 3). It underwent a total axial elongation of 4.9 mm, at which point ductile fracture occurred. The onset of necking appeared at an engineering stress of $S_e = 363.85$ MPa and an engineering strain of $e = 1.4\%$, produced at a force of $F = 10.3$ kN; the axial displacement registered during test was about 0.42 mm. The strength coefficient and the strain-hardening exponent used to plot the RSS curve were respectively $k = 391.5$ MPa and $\varepsilon_N = 0.014$. For this sample, the onset of necking began almost immediately after the elastic range. When processing the FP + 2D-DIC data, necking started at the 3rd load stage at one position, but then moved to another position and was re-initiated at the 5th load stage.

3. Image processing

The deformation experienced by the specimen when subjected to successive load stages was measured using the combined 2D-DIC and FP technique with the experimental set-up is shown in figure 1. In order to perform 2D-DIC, ncorr-V1.2 open source program for MATLAB has been used [26].

One RGB image, $\mathbf{I}_s = \mathbf{I}_{R,s} + \mathbf{I}_{G,s} + \mathbf{I}_{B,s}$ of size $M \times N \times 3$ at each deformation stage (load case $s = 1, 2, \dots, S$) was acquired. The red speckle pattern painted on the specimen and used for 2D-DIC can be observed through the B channel ($\mathbf{I}_{B,s}$) and the blue and red projected fringe pattern used for FP can be observed through the R channel ($\mathbf{I}_{R,s}$), as shown in figures 4(a) and (b), which provides an example of the image of the load stage $s = 56$ (last stage just before breaking point of specimen 1) with a size of $M = 239$ and $N = 1009$ pixels. The size of the subset used for DIC depends of the speckle size (e.g. in this work a subset size of 16×16 pixels for a speckle size of about 1 to 5 pixels).

3.1. In-plane displacements, measurements and corrections

By performing 2D-DIC on the speckle images of the specimen surface at a load stage s , each displaced pixel within the region of interest (\mathbf{O}_s) of the speckle image ($\mathbf{I}_{B,s}$) is searched in the image at the previous load stage of the specimen ($\mathbf{I}_{B,s-1}$), as

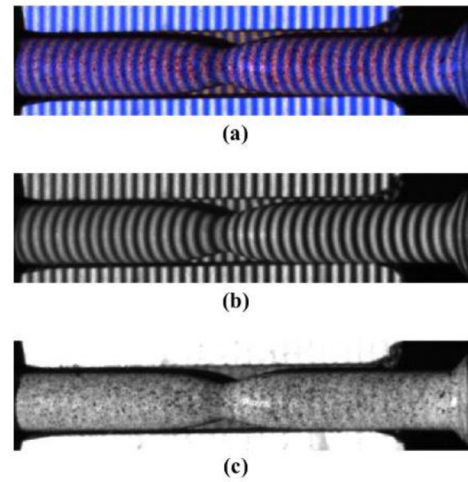


Figure 4. (a) Example of acquired image (\mathbf{I}_s) for $s = 56$; (b) corresponding R-channel image ($\mathbf{I}_{R,s}$); (c) corresponding B-channel image ($\mathbf{I}_{B,s}$).

shown in the example given in figure 5. The region of interest is a mask taking the value one for the pixels that contain information (i.e. on the specimen surface), otherwise zero, defined manually for each image at each load stage. 2D-DIC then finds the position of the pixel *before* it has been displaced due to the applied load. Thus, at each load stage, the initial (designed with subscript 1) and final positions (designed with subscript 2) of each surface element (i, j) corresponding to a pixel of the visualized specimen surface are computed, being:

- i. $x_2(i, j)$ and $y_2(i, j)$, the matrix elements of the pixel positions within the image $\mathbf{I}_{B,s}$ in the x - and y -directions after the load stage. These matrices are respectively rows $[1 \ 2 \ 3 \ \dots \ N]$ repeated M times and columns $[1 \ 2 \ 3 \ \dots \ M]$ repeated N times.
- ii. $\Delta x'_s(i, j)$ and $\Delta y'_s(i, j)$, the corresponding computed in-plane displacements in pixels of the pixels (i, j) at the load stage s , with respect to their positions at the previous load stage $s - 1$. For the first load stage ($s = 1$), in-plane displacements are set to zero. Figure 6 shows the in-plane displacements at $s = 56$. The computed displacements have a sub-pixel resolution of ± 0.05 pixels.
- iii. The matrices of the pixel positions within image $\mathbf{I}_{B,s-1}$, prior to the deformation stage s , are obtained as follows:

$$\begin{aligned} x_{1,s}(i, j) &= \lfloor x_2(i, j) - \Delta x'_s(i, j) \rfloor \\ y_{1,s}(i, j) &= \lfloor y_2(i, j) - \Delta y'_s(i, j) \rfloor \end{aligned} \quad (5)$$

where $\lfloor \cdot \rfloor$ denotes that the value is rounded to the next integer pixel positions for $(x_{1,s}, y_{1,s})$ because of the sub-pixel resolution of the 2D-DIC algorithm.

Two corrections must be applied to these obtained $\Delta x'_s$ and $\Delta y'_s$ values:

During the image acquisition at the different load stages, rigid body displacements ($\Delta x'_{s,rb}$ and $\Delta y'_{s,rb}$) may happen (when the whole specimen displaces relative to the camera). This is corrected by subtracting the displacements obtained by performing 2D-DIC on a single reference pixel (i_r, j_r). It is

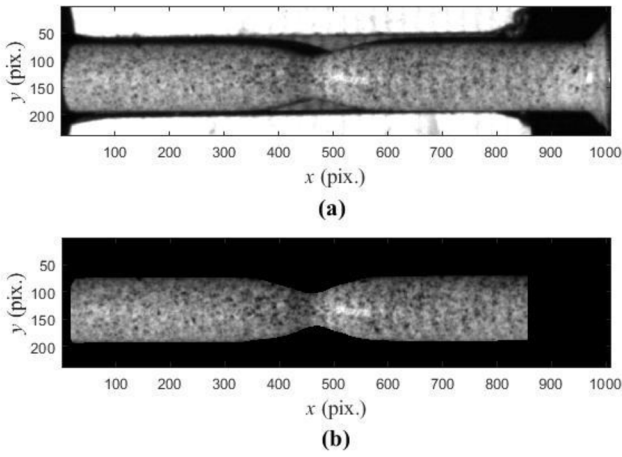


Figure 5. Example of two consecutive speckle images for $s = 56$: (a) $I_{R,s-1}$ and (b) $I_{R,s}$, the displaced speckle image multiplied by the region of interest matrix (O_r).

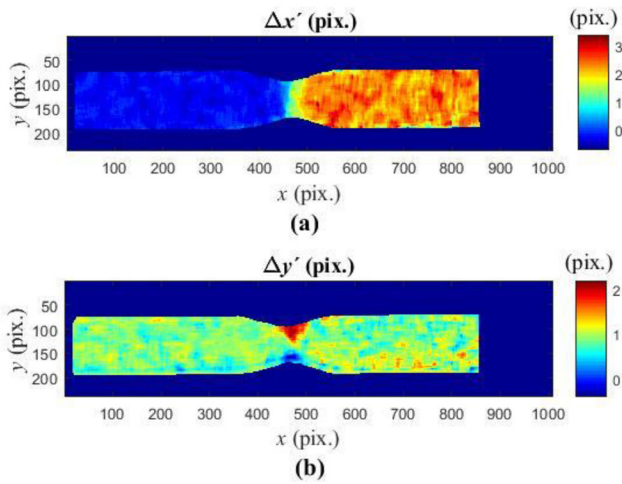


Figure 6. Mapping of in-plane displacements ($\Delta x'_s$ and $\Delta y'_s$) obtained by applying 2D-DIC to the images shown in figure 5.

known beforehand, that this reference pixel is not subjected to any deformation between the consecutive load stages (e.g. a pixel next to the fixed specimen grip)

$$\begin{aligned} \Delta x'_{s,c} &= \Delta x'_s - \Delta x'_{s,rb}(i_r, j_r) \\ \Delta y'_{s,c} &= \Delta y'_s - \Delta y'_{s,rb}(i_r, j_r). \end{aligned} \quad (6)$$

The obtained *in-plane* displacement of the surface elements is affected by their *out-of-plane* positions (if no telecentric lens is used). For this correction, the out-of-plane distances $z_{1,s}$ and $z_{2,s}$ are required. These are the distances of the specimen surface elements (before and after being displaced, respectively) with respect to a flat reference surface perpendicular to the optical axis of the lens. Also, the following parameters are required: the inverse of the lateral magnification of the lens at the reference plane, L , the distance z_0 from the reference surface to the camera and the relative distance of each surface element to the optical axis, which can be approached by the distance to the centre of the image (x_{0A} , y_{0A}). The in-plane correction for each pixel displaced to (x_2, y_2) is then given by the following equation:

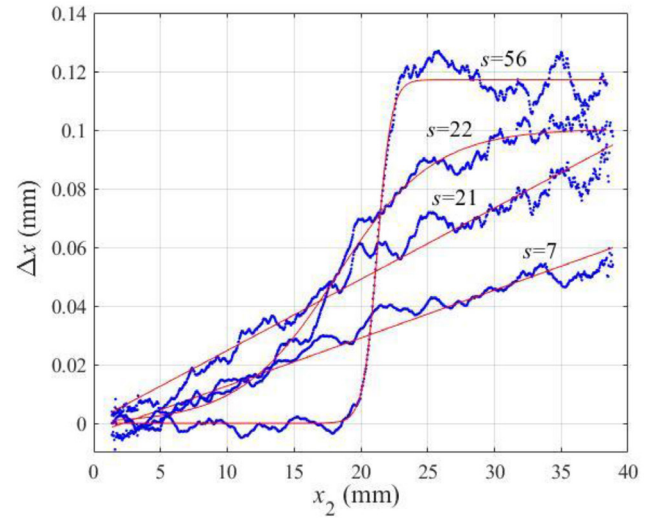


Figure 7. Example of profiles of the displacements in the axial direction between consecutive load stages, Δx_s , for several load stages s . The green continuous lines are the corresponding fitting results of equation (13) to the experimentally obtained data.

$$\Delta x_s = L \cdot \left[\Delta x'_{s,c} + \left((x_2 - x_{0A}) \frac{z_{2,s}}{z_0} - (x_{1,s} - x_{0A}) \frac{z_{1,s}}{z_0} \right) \right], \quad \text{for } s = 2, S, (7)$$

Distortion effects were neglected because measurements were made close to the optical axis of the lens.

The same equation is valid for the y -direction. L is given in mm/pixel and the corrected displacements are given in mm. For example, for the 1st experiment introduced in this paper, $(x_{0A}, y_{0A}) = (468, 132)$, $L = 0.045$ mm/pixel and $z_0 = 329$ mm. Details of calibration process to obtain these parameters are given in [25]. Nevertheless, since the out-of-plane distances (maximum value of 3 mm) are much smaller than z_0 , the second correction is negligible in our experiments and $\Delta x_s \cong L \cdot \Delta x'_{s,c}$ (the mean of the absolute value of the differences is $6 \cdot 10^{-4}$ mm).

Figure 7 shows an example of averaged Δx_s profiles along the x - or axial load direction (averaged in the y -direction over several measured profiles at each load stage s) obtained for specimen 1. Besides the noise (standard deviation of about ± 0.012 mm, corresponding to a oscillation between 1 and 4,4 pixels), it can be observed that for initial loading stages ($s < 22$) the values of Δx_s increase linearly with x_2 and therefore the deformation is homogeneously distributed along the specimen length of the observed area (the stress state is uniform and uniaxial over the entire specimen volume). For higher loading stages ($s \geq 22$), there is no longer linear behaviour and the slope of the profile becomes practically zero everywhere, except at a decreasingly smaller zone, where all deformation is concentrated corresponding to the necking zone. This load stage, at which the transition to non-uniform axial deformation starts to appear, is designed s_N .

3.2. Out-of-plane displacements

The out-of-plane displacements or z -positions were obtained using the FP technique on the fringe images of the R-channel

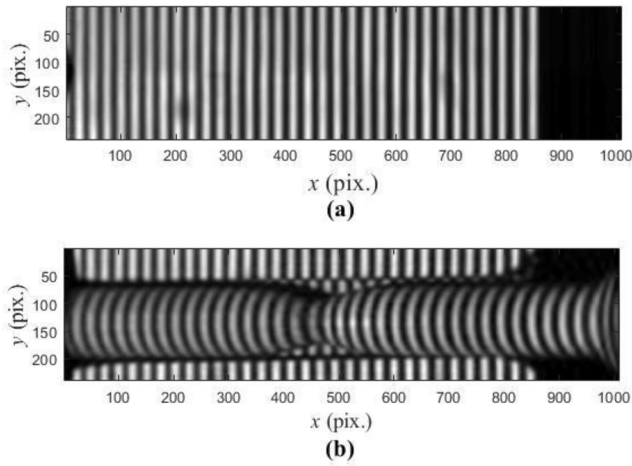


Figure 8. (a) Reference fringe image (I_0). (b) Example of specimen fringe image ($I_{R,s}$) at $s = 56$.

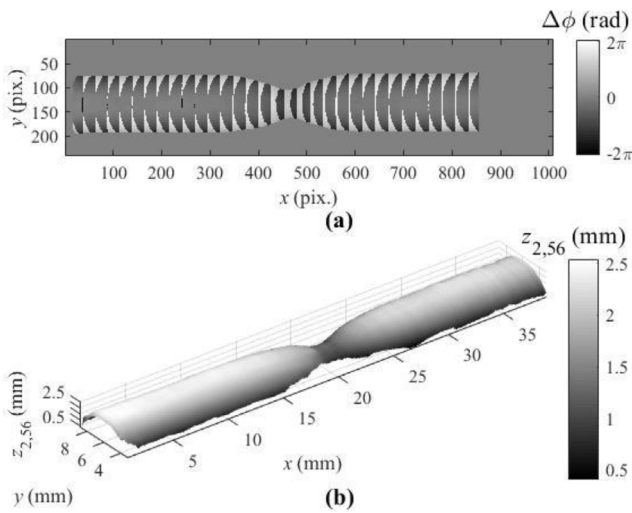


Figure 9. (a) Wrapped phase difference map between the two previous fringe images. (b) z -positions in mm obtained from the calibrated unwrapped phase map.

($I_{R,s}$), where the shifted phase of the projected fringes relative to the straight fringes corresponding to the plane reference surface (I_0) was calibrated and related to z -positions (in mm) using a second-order polynomial, the coefficients of which were obtained through a calibration process [25]. At any load stage s , the matrix elements of the z -positions of the pixels $z_{2,s}(i,j)$ were obtained. An example of $I_{R,s}$ and I_0 at load stage $s = 56$ is shown in figures 8(a) and (b), respectively). Figure 9(a) shows the wrapped phase difference ($\Delta\phi$) directly obtained by the application of the FP algorithm to the two previous fringe images. Figure 9(b) represents the corresponding z -positions of the surface elements computed from the unwrapped and calibrated phase map.

To obtain the displacements in the z -direction that each pixel (i,j) has experienced after each load stage $s = 2, 3, \dots$, it is necessary first to obtain the z -positions, $z_{1,s}(i,j)$, in the previous stage, as follows:

$$z_{1,s}(i,j) = z_{2,s-1}(x_{1,s}, y_{1,s}) \quad \text{for } s = 2, 3, \dots, S. \quad (8)$$

For $s = 1$, before applying the first load stage, there is no change in the out-of-plane displacement: $z_{1,1}(i,j) = z_{2,1}(i,j)$. For the following load stages, the out-of-plane displacements experienced by each pixel are given by:

$$\Delta z_s(i,j) = z_{2,s}(i,j) - z_{1,s}(i,j) \quad \text{for } s = 2, 3, \dots, S. \quad (9)$$

3.3. Total displacements

The total displacements or accumulated displacements at each load stage, s , are calculated as before, by tracking back the displaced pixels of all the previous load stages. The values are calculated iteratively as follows:

$$\begin{aligned} \Delta x_{T,s}(i,j) &= \Delta x_s + \Delta x_{T,s-1}(x_{1,s}, y_{1,s}) \\ \Delta y_{T,s}(i,j) &= \Delta y_s + \Delta y_{T,s-1}(x_{1,s}, y_{1,s}) \quad \text{for } s = 2, 3, \dots, S, \\ \Delta z_{T,s}(i,j) &= \Delta z_s + \Delta z_{T,s-1}(x_{1,s}, y_{1,s}) \end{aligned} \quad (10)$$

where $\Delta x_{T,1} = \Delta y_{T,1} = \Delta z_{T,1} = 0$

As mentioned in the second section of this paper, the applied force for each total x -displacements and the force-elongation values obtained with the GÜNT system are as shown in figure 3.

4. Determination of the Bridgman's necking parameters

The onset of necking appears when the homogeneous deformation no longer happens in the axial load direction (x -direction), i.e. when Δx_s is no longer linear with x . This can clearly be seen in figure 7 at the deformation stage $s_N = 22$ and coincides with Considère's criterion for the ultimate stress, as shown in figure 3.

4.1. Using in- and out-of-plane displacements

The FP + 2D-DIC technique makes it possible to determine the shape of the specimen or position of each surface element after each loading stage, $z_{2,s}$, measured at the positions (x_2, y_2), which have to be multiplied by the lateral magnification, L , to have the same units (no longer in pixels) and the total displacements in each spatial direction given in equation (10).

4.1.1. Before necking. Before necking ($s < s_N$), there is a slight decrease in the specimen radius, r_s , with the increasing load. The radius is obtained by fitting a half circle to the mean z -positions of the specimen's surface elements along the specimen's loading axis, as follows:

$$z_{\text{fit},s}(r_s, y_{0,s}, z_{0,s}) = \sqrt{r_s^2 - (y_2 - y_{0,s})^2} + z_{0,s}, \quad (11)$$

where $(y_{0,s}, z_{0,s})$ is the centre of the half circle. Figure 10 shows two of these fitted half circles. The nonlinear least squares formulation is used to fit the half circle to the experimental data [27]. An initial estimation for $(r_s, y_{0,s}, z_{0,s})$ is necessary for the iterative approach, which is guided by a trust region fitting algorithm. Only the initial estimation for $s = 1$

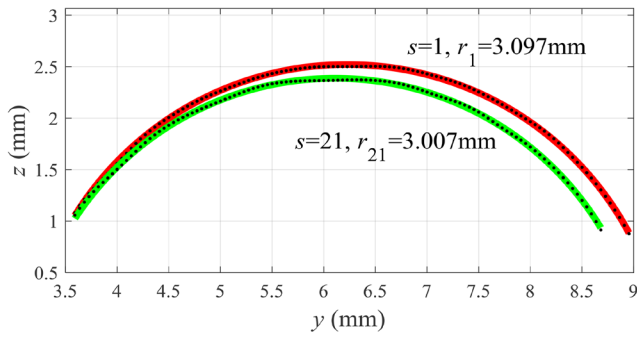


Figure 10. Examples of half circle fitting (continuous lines) to the experimental data (dots) to obtain the specimen radius before necking for $s = 1$ and $s = 21$.

has to be introduced manually; the following fittings use the resulting fitted parameters of the previous fitting process as initial estimations.

4.1.2. After necking. After necking ($s \geq s_N$), the specimen shape is no longer cylindrical and to estimate the TSS curve, the following Bridgman's parameters are defined: the *radius of curvature* of the necking zone, $R_{N,s}$, and the minimum radius of the smallest cross-section area or *necking radius*, $r_{N,s}$. To estimate these parameters from $z_{2,s}$, a nonlinear least square fitting process is performed; as a fitting function, a ring torus function (according to Bridgman) with torus radius $R_{N,s}$ and radius of revolution $R_{N,s} + r_{N,s}$ is used, which can be defined as follows:

$$z_{\text{fit},s}(R_{N,s}, r_{N,s}, y_{N,s}, z_{N,s}) = \sqrt{\left| R_{N,s} + r_{N,s} - \sqrt{R_{N,s}^2 - (x_2 - x_{N,s})^2 - (y_2 - y_{N,s})^2} \right|} + z_{N,s} \text{ for } s = s_N, \dots, S \quad (12)$$

where $(R_{N,s}, r_{N,s}, y_{N,s})$ and $z_{N,s}$ will be the fitting coefficients of the fitting process to the values of $z_{2,s}$ at positions (x_2, y_2) and $(x_{N,s}, y_{N,s}, z_{N,s})$, which are the coordinates of the centre of the torus or necking point. For the fitting of this function, it is necessary to undertake the following steps:

- i. Delimit and define the zone around the necking used for the fitting of equation (12). This zone can be identified using the x -displacement profiles, but it is not clearly delimited, as shown in figure 7. To delimit it and the corresponding data points to which the torus will be fitted, we propose selecting the data for which the derivatives of the total x -displacements are within a bandwidth, close around the maximum slope of the total x -displacements, which happens at the necking position, $x_{N,s}$.
- ii. Estimate the value of $x_{N,s}$.

To calculate a noise free derivative of the total x -displacements and at the same time estimate $x_{N,s}$, the following simple function is proposed as an *in-loading direction* displacement model:

$$\Delta x_{\text{fit},s}(x_{N,s}, \alpha'_s, \beta'_s) = \frac{\alpha'_s}{1 + e^{-\beta'_s(x_2 - x_{N,s})}} \text{ for } s = s_N, \dots, S \quad (13)$$

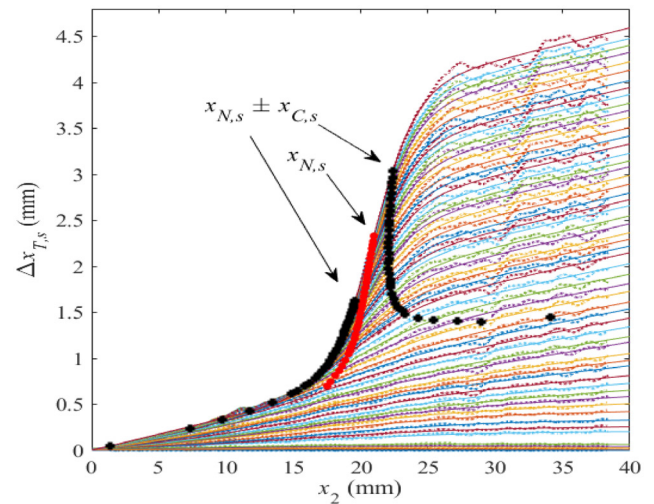


Figure 11. The average and fitted profiles of $\Delta x_{T,s}$ along the x -axis.

where α'_s is the maximum displacement and $0, 25\alpha'_s\beta'_s$ is the slope at the necking point $x_{N,s}$. Examples of some fitting profiles are shown in figure 7. For the total x -displacements, it is necessary to account also for the homogeneous displacements before the necking takes place; the final model proposed to be fitted to these profiles is then:

$$\Delta x_{T,\text{fit},s}(x_{N,s}, \alpha_s, \beta_s, \gamma_s) = \frac{\alpha_s}{1 + e^{-\beta_s(x_2 - x_{N,s})}} + \gamma_s \cdot x_2 \text{ for } s = 1, \dots, S \quad (14)$$

where $x_{N,s}, \alpha_s, \beta_s$ and γ_s are the fitting coefficients, being γ_s the slope of the linear part of the function. These coefficients are obtained by fitting equation (14) to the experimentally obtained total x -displacement profiles using a nonlinear least squares formulation. Figure 11, as an example, shows all the fitted *total* x -displacement profiles obtained from a sequence of 56 images acquired from steel specimen during the tensile test, before and after necking, until the break. This figure shows a biased noise in the unfitted total displacement measurements, this is due to the propagation of the errors (standard deviation of ± 0.012) between each load stage and the previous one. Nonetheless the fitting of the proposed displacement model behaves as expected.

The criteria proposed for determining how many data points around the necking position, $x_{N,s}$, is extracted from the derivative of equation (14), which is a symmetrical distribution with the maximum at the necking zone. When this derivative is ' μ ' times the maximum value (with $\mu < 1$), the cutting positions around $x_{N,s}$ are obtained for each load stage, s , as follows:

$$x_{c,s} = \frac{1}{\beta_s} \cdot \arccos \frac{\alpha_s \beta_s (2 - \mu) + 4\gamma_s}{\mu \alpha_s \beta_s - 4\gamma_s}. \quad (15)$$

The necking zone can then be limited to the interval:

$$x_2 = [x_{N,s} - x_{c,s}, x_{N,s} + x_{c,s}]. \quad (16)$$

The most adequate value for μ is $\mu = 0.9$ because it provides the smallest necking zone with enough data points for estimating the Bridgman's parameters. Figure 11 also shows the

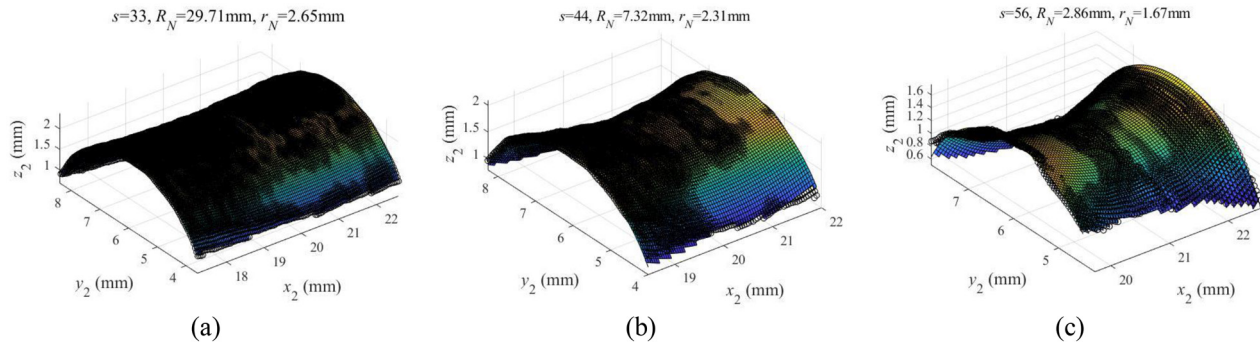


Figure 12. Examples of torus fitting results to obtain the curvature of the necking zone ($R_{N,s}$) and the necking radius ($r_{N,s}$) for: (a) $s = 33$, (b) $s = 44$ and (c) $s = 56$.

corresponding estimated necking position and zone for $s \geq s_N$. The experimental data are represented by dotted lines and the continuous lines are the fitting results of equation (12). For $s \geq s_N$, the red dots show the necking positions and the black crosses represent the limits of the necking zone interval, that will be used to estimate the Bridgman parameters.

Now, the curvature of the necking zone, $R_{N,s}$, and the necking radius, $r_{N,s}$, can be obtained by once again introducing a nonlinear least square fitting process of the torus function of equation (12) to the values of $z_{2,s}(x_2, y_2)$, belonging to the defined necking zone. Some examples of torus fitting results are shown in figure 12.

The fitting results for the necking radius before (equation (11)) and after (equation (12)) and the radius of curvature of the necking zone are shown in figures 15 and 16 at each loading stage.

4.2. Using in-plane displacements only

An alternative and simpler way of obtaining the necking radius and the curvature radius from in-plane displacements only (obtained using 2D-DIC) is proposed by considering no changes in the specimen's volume when it is deformed.

The specimen before being subjected to a deformation is supposed to be divided into slices of arbitrary small thickness, x_0 and radius, r_0 , perpendicular to the loading axis (x -axis). When the specimen is deformed, the slices change their thickness (δx) and radius (δr), but not their volume. Thus, for each slice:

$$\pi(r_0 + \delta r)^2(x_0 + \delta x) = \pi r_0^2 x_0. \quad (17)$$

From this equation the radius of the slices when deformed in the x -direction changes to:

$$r_0 + \delta r = r_0 \sqrt{\frac{x_0}{x_0 + \delta x}} = r_0 \sqrt{\frac{1}{1 + e_x}} \quad (18)$$

where $e_x = \delta x/x_0$ is the engineering strain for each slice.

This axial strain can be obtained from the total x -displacements experienced by the surface elements Δx_T , comprising the total relative displacement of a surface element (i.e. pixel) with respect to the surface elements, for which there is no x -displacement (in our experiment the pixels of the

left end of the specimen). Before necking, Δx_T increases linearly along the x -axis because all the pixels undergo the same deformation. After necking, the deformation starts to concentrate around x_N and the relative x -displacement of the surface elements along the x -axis is empirically obtained from equation (14) of the total displacements. No distinction between load stages, before and after necking should be done, because equation (14) includes the pre-necking behaviour. Therefore, the sub-index ' s ' will be obviated in the following equations.

The experiments deliver the total relative displacements of each pixel after being displaced to the position x_2 ; these pixels are separated by a constant distance, P , which is related to the distance between the pixels before being displaced, x_0 , as follows: $P = x_0 + \delta x$. The derivative of Δx_T , for small P , is then related to the axial strain in the following way:

$$\frac{d}{dx^2} \Delta x_T \approx \frac{\Delta x_T(x_2 + P) - \Delta x_T(x_2)}{P} = \frac{\delta x}{x_0 + \delta x} = \frac{e_x}{1 + e_x}. \quad (19)$$

The derivative of equation (14) delivers:

$$\frac{d}{dx^2} \Delta x_T \approx \frac{\frac{1}{4}\alpha\beta}{\cosh^2\left[\frac{\beta}{2}(x_2 - x_N)\right]} + \gamma. \quad (20)$$

With equations (19) and (20), the engineering strain for each slice results in:

$$e_x = \frac{\frac{d}{dx^2} \Delta x_T}{1 - \frac{d}{dx^2} \Delta x_T} = \frac{\frac{1}{4}\alpha\beta + c \cosh^2\left[\frac{\beta}{2}(x_2 - x_N)\right]}{(1 - \gamma) \cosh^2\left[\frac{\beta}{2}(x_2 - x_N)\right] - \frac{1}{4}\alpha\beta}. \quad (21)$$

Replacing equation (21) in (18), the radius of the slices at x_2 , after experimenting their corresponding x -deformation, is obtained as follows:

$$r(x_2) = r_0 + \delta r = r_0 \sqrt{1 - \frac{\frac{1}{4}\alpha\beta}{\cosh^2\left[\frac{\beta}{2}(x_2 - x_N)\right]} - \gamma}. \quad (22)$$

In particular, a simple necking radius at $x_2 = x_N$, is obtained as follows:

$$r_N = r_0 \sqrt{1 - m}, \quad (23)$$

where $m = 0, 25\alpha\beta + \gamma$ is the slope of Δx_T at x_N . Thus, the necking radius can be estimated from the fitting parameters of

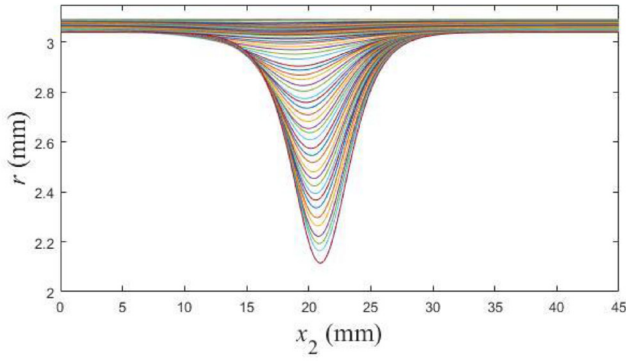


Figure 13. The radius of the specimen obtained with equation (22) along the x_2 -axis.

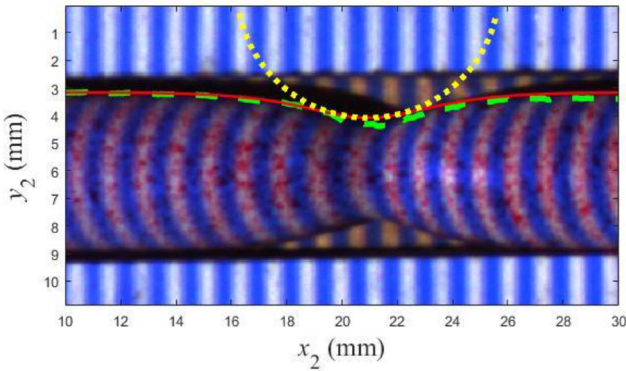


Figure 14. Example of the experimental profile obtained using equation (9) (discontinuous green line) and equation (22) (red continuous line) and curvature radius using equation (25) (yellow dotted line).

the total axial displacements by using the empirically obtained equation (14).

Figure 13 shows the radii of all slices of the specimen along the longitudinal axis for all load stages. The evolution of the displacement of each slice and the specimens profile obtained using equation (22) with increasing load stages are shown in a video available in the online supplementary information.

The curvature radius of the necking zone, R_N , can also be estimated by equalling the Taylor-series expansion of equation (22) around x_N , with the Taylor-series expansion of a half circle $\tilde{r}(x_2)$:

$$r(x_2) \approx r_0\sqrt{1-m} + \frac{r_0\alpha\beta^3}{32\sqrt{1-m}}(x_2 - x_N)^2, \quad (24)$$

$$\tilde{r}(x_2) \approx r_c - \sqrt{R_N^2 - (x_2 - x_N)^2} \approx r_c - R_N + \frac{1}{2R_N}(x_2 - x_N)^2 \quad (25)$$

where (x_N, r_c) is the centre of the half circle. By equalling the second-order terms, we get:

$$R_N = \frac{16\sqrt{1-m}}{r_0\alpha\beta^3}, \quad (26)$$

and by equalling the first term, we confirm that $r_c = R_N + r_N$.

Figure 14 shows an example of profiles of the sample obtained at the last load stage, using experimental data from

figure 11, the profile obtained with equation (22) and the curvature radius obtained by using equation (26).

5. Results of axial average stress curve at the smallest cross section and equivalent stress–strain curve obtained from 2D-DIC + FP values

The results of the two proposed ways (using the 3D data and using the data of the total AD profiles) to obtain the values of the minimum radii, r_s and $r_{N,s}$, in the case of necking formation, and the necking curvature, R_N , are shown in figures 15 and 16, respectively, for the different load stages and for two specimens presenting necking formation (steel and Cu bar). Figure 15 shows the minimum radius obtained for another specimen of Al, in which no necking appeared during the tensile test.

Before necking, quite good agreement is observed for the minimum radius for all specimens (steel, Al and Cu specimens). For the Cu bar and especially for the steel bar, there is an increasing difference with increasing load after necking (at $\Delta x_{T,s=22} = 1.66$ mm and at $\Delta x_{T,s=5} = 0.42$ mm for steel and Cu, respectively). The r_N values obtained from AD are always higher, about 0.15 mm at the last load stage for steel and about 0.1 mm for copper, which represents a difference of about 7.5% and 5% in the smallest necking radius obtained with torus fitting of the 3D data for steel and Cu, respectively.

For the necking curvature, there is an appreciable difference between the values obtained with the two methods (figure 16(a)) for the specimens (steel and Cu), which presented necking formation. The values for R_N obtained with AD are in both cases higher, especially at the beginning of the necking and when approaching the ductile fracture.

In figure 16(b) the ratio r_N/R_N with respect the average strain at the smallest cross section is shown. When obtained with the approach that uses AD data, it is observed that the necking curvature (R_N) is getting faster smaller for steel than for Cu with increasing average strain at the smallest cross section, which means that the necking formation is restrained to a smaller region in steel than in Cu. However, this is not appreciable when using 3D data, and this tendency can therefore not yet be confirmed. In general, in [7] this graphical representation was also obtained for several materials from FEM analysis and from experimental data of different steel types, showing a good coincidence with our results.

For our proposal with regard to obtaining the equivalent stress–strain curve of equation (3) after the onset of necking, the effect of an error in the estimation of R_N does not exert as great an effect as in the estimation of r_N because there is a dependence of the curve with the inverse of the area of the smallest cross section ($A = \pi r_N^2$). The noise in the estimation for r_N will be amplified when calculating the corresponding smallest cross section, which is then transmitted to the average true stress (F/A), to the Bridgman's stress $C \cdot (F/A)$ and to the average strain $Ln(A_0/A)$. This can be appreciated in the respective curves designated with $ASSI_{3D}$ and $BSSI_{3D}$ in figures 17(a) and (b) for the steel and Cu specimens, where the sub-index 3D denotes that they have

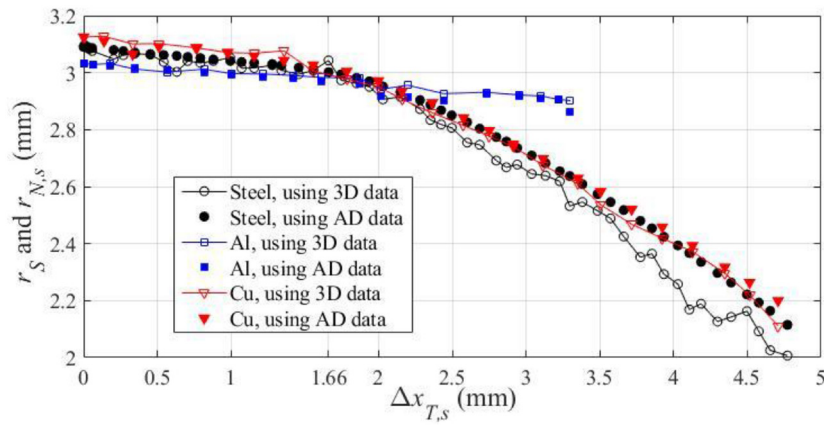


Figure 15. Minimum specimen radius (r_s , before necking and after necking $r_{N,s}$) using both estimation methods (using 3D or AD data).

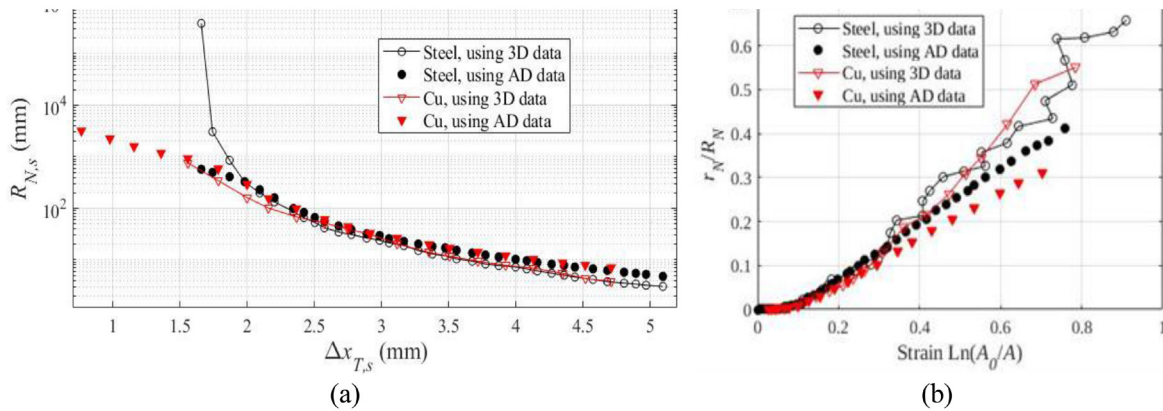


Figure 16. (a) Radius of curvature of necking for the two specimens (steel and Cu) and the two proposed estimation methods (using 3D or AD data). (b) Evolution of the r_N/R_N ratio with the strain for both materials and approaches.

been obtained using torus fitting of the 3D data. In the same figure, the curves $ASS|_{AD}$ and $BSS|_{AD}$ are also represented, where the sub-index AD denotes that they were obtained using the proposed equations (23) and (26) derived from the total AD profiles. As can be observed, both samples present a large deformation after necking formation but then behave in quite different ways. Both stresses ASS and BSS (obtained with 3D and AD data) at the smallest cross section of the steel bar increases slow but steadily during the necking formation until rupture, while the Cu bar shows a decrease in the stresses at about the strain of 0.3. This result appoints for a smaller stress concentration in Cu probably distributed over a larger necking zone than for the steel sample. This is in accordance with having a larger necking curvature radius (for a certain necking radius), since it starts to increase over the steel curvature radius (for the same necking radius) at about the same strain of 0,3 as can be appreciated in figure 16(b).

The stress strain curves obtained with the 3D data, although noisier, is supposed to be closer to the real stress strain curve obtained from the equation (23) since it considers the experimentally obtained necking curvature (i.e. without the approach of volume conservation). Therefore, the curves $ASS|_{3D}$ and $BSS|_{3D}$ can be used to estimate the error of the $ASS|_{AD}$ and $BSS|_{AD}$ curves. Furthermore, it is noticeable that the curves $ASS|_{AD}$ and $BSS|_{AD}$ remain below their respective $ASS|_{3D}$ and $BSS|_{3D}$ curves for all load stages; their estimated

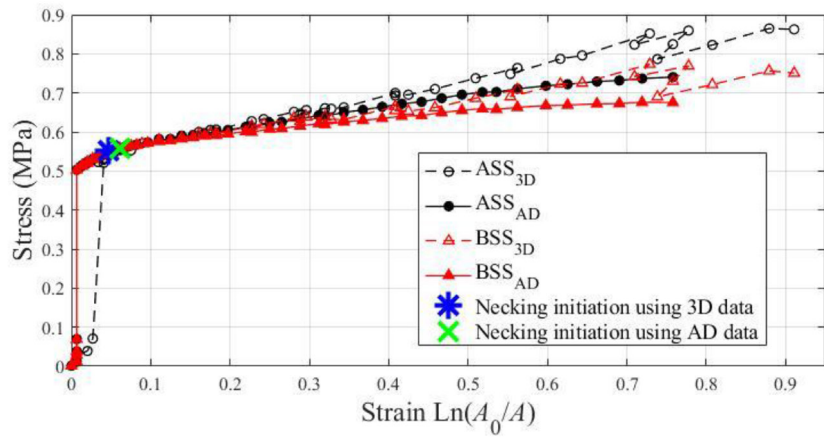
values of stress and strain are lower, thus, anticipating the ductile rupture of the specimen.

The errors committed for the BSS curves are shown in figure 18 for the different load stages (note that in the case of the Cu specimen, finite R_N values using torus fitting are obtained a few steps after the initiation of necking, at $s = 9$). The error was calculated as follows, taking the sign into account:

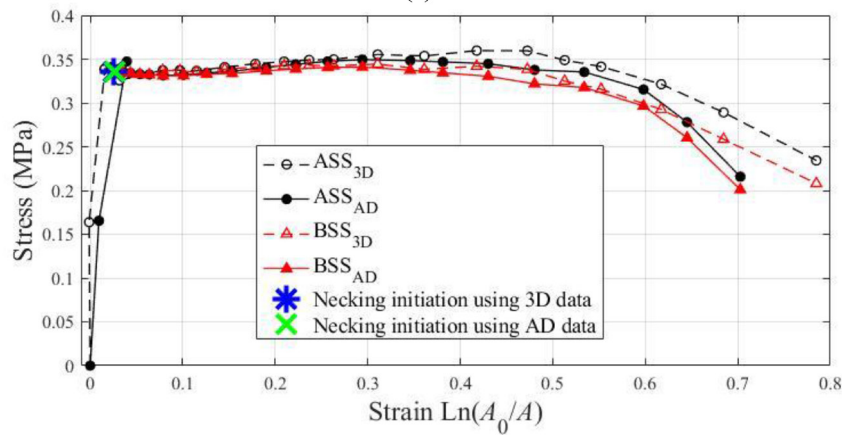
$$\xi(\%error) = 100 \frac{BSS|_{3D} - BSS|_{AD}}{BSS|_{3D}}. \quad (27)$$

Figure 18 shows the average tendency of the mean error and their standard deviations. For the Bridgman's stress values in steel, we obtain an underestimated value using AD of about $11.5 \pm 2.7\%$ for the ductile fracture and this decreases to $-0.8 \pm 2.7\%$ for the initiation of necking. For the strain values obtained with AD, we determined that they are also underestimated by about $28 \pm 8.7\%$ for ductile fracture, decreasing to about $6 \pm 8.7\%$ for the necking initiation. For the Bridgman's stress and strain for the Cu specimen, we obtain for all load stages an underestimated value using AD of $1.2 \pm 1.2\%$ for Bridgman's stress and $10 \pm 6.2\%$ for the strain.

The estimated error is in accordance with errors observed in [7], which predicts values between 2.6% and 10.6% in the evaluation of Bridgman's equivalent stress for different materials.

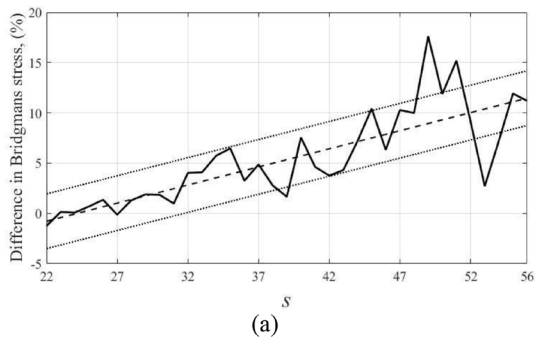


(a)

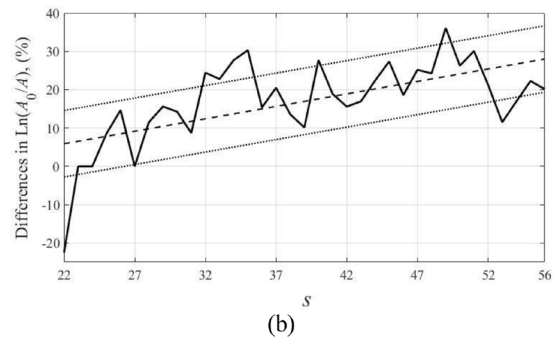


(b)

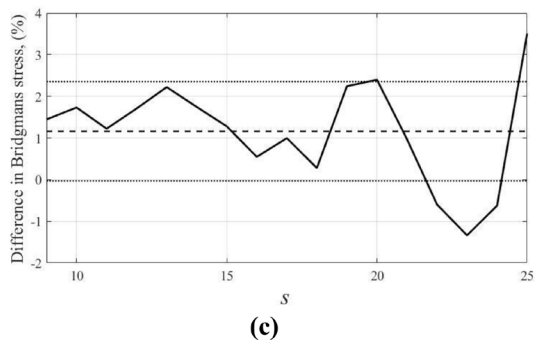
Figure 17. Average axial true stress at the smallest cross section area and equivalent stress–strain curve for (a) steel specimen and (b) Cu specimen.



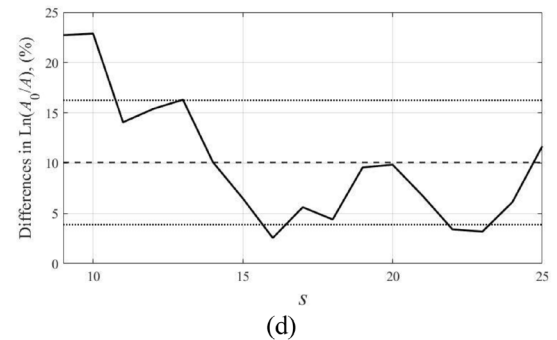
(a)



(b)



(c)



(d)

Figure 18. Error in the estimation of Bridgman's stress and strain using AD data relative to the estimated result using 3D data, for the steel specimen ((a) and (b)) and for the Cu specimen (c) and (d).

6. Discussion and conclusions

The main problem in determining the Bridgman's stress–strain curve after necking initiation is the correct estimation of the Bridgman's parameters, r_N and R_N . The problem in the estimation of the necking curvature (R_N) is that the real necking profile does not exactly coincide with a half circle, and the determination of the smallest necking radius (r_N) has to be very precise because its value greatly affects both the stress and the average true strain. The main proposal of the present work is to estimate these parameters experimentally in a convenient and feasible way, suitable for use for engineering purposes.

One possibility is to obtain these parameters from the 3D displacement measurement maps of the specimen's surface at the necking zone. For this, we propose using an alternative technique to 3D-DIC, namely a combination of 2D-DIC and FP. We consider this to be much easier to develop as a 'home-made' technique. Detailed information on the set-up and calibration is given in a few references and detailed explanations of the data processing for our purpose are given in the present work. The initiation of necking is then detected when the axial displacement map is no longer uniform, and the location of the minimum necking radius is determined from the position of the maximum slope of the axial displacement, which can be well-fitted with equation (13). Therefore, the onset of necking is identified accurately. The 3D shape of the necking zone is obtained from the out-of-plane displacements acquired by FP. The 3D data points obtained around the necking zone result in a shape that does not quite fit with a torus, making the determination of R_N ambiguous.

Therefore, we delimit the zone around the necking location with equation (15) in a convenient way through a parameter μ . The torus function given by equation (12) is then fitted to the 3D data of this necking zone, obtaining the estimated values for r_N and R_N . Nonetheless, the values obtained for r_N are noisy, affecting the values of the minimum cross section area and the derived average TSS and Bridgman's stress–strain curves (designated $ASSI_{3D}$ and $BSSI_{3D}$). The curves obtained provide a useful range of estimated stress–strain values for the plastic behaviour of the specimens.

An alternative easier approach for determining the Bridgman's parameters is also proposed. This is derived from only the AD values obtained with 2D-DIC, considerably reducing the experimental and computational complexity. The good fitting of equation (14) to the total axial displacements (shown in figure 11) makes it possible to derive an equation (22) for the radius of the specimen along the loading axis. For this approach, the conservation of volume is assumed. In particular, the minimum radius at the necking location is obtained (equation (23)). Applying a simple Taylor expansion around the necking location, equation (26) for the local curvature radius R_N is formulated. The fitting of equation (14) provides smooth values for both r_N and R_N , resulting in a smooth variation of the average TSS and Bridgman's stress–strain curves (designated $ASSI_{AD}$ and $BSSI_{AD}$). In particular, the smooth ratio r_N/R_N versus average strain at the smallest cross section, allows to appreciate

possible differences in the extension of the necking zone for a given average strain for different materials. It was observed, for instance, that Cu presented a larger extension of the necking zone than steel for average strain values higher than about 0,3, the same strain for which ASS and BSS started to decrease, probably because the stress concentrated at the smallest cross section is being distributed over the necking zone while, for the steel sample, the ASS and BSS continuously increased producing an increasing stress concentration at the smallest cross section with increasing average strain values, until fracture.

Finally, the $ASSI_{AD}$ and $BSSI_{AD}$ curves are below the $ASSI_{3D}$ and $BSSI_{3D}$ curves for the two studied samples presenting necking formation. The difference depends on the specimen's material. Considering that the $ASSI_{3D}$ and $BSSI_{3D}$ curves are closer to the real plastic behaviour of the material, the $ASSI_{AD}$ and $BSSI_{AD}$ curves estimate the stress and strain values below the real values, allowing the anticipated prediction of ductile fracture.

Acknowledgments

We thank Prof. Sancho Salcedo (PhD) for discussions and revision of the manuscript content.

Conflicts of interest

The authors declare no conflict of interest.

ORCID iDs

Cristina Alén-Cordero  <https://orcid.org/0000-0002-9097-7776>

References

- [1] Malesa M, Malowany K, Tomczak U, Siwek B, Kujawinska M and Sieminska-Lewandowska A 2013 Application of 3D digital image correlation in maintenance and process control in industry *Comput. Ind.* **64** 1301–15
- [2] Bolhassani M, Hamid A A, Rajaram S, Vanniamparambil P A, Bartoli I and Kotsos A 2017 Failure analysis and damage detection of partially grouted masonry walls by enhancing deformation measurement using DIC *Eng. Struct.* **134** 262–75
- [3] Ling Y 1996 Uniaxial true stress–strain after necking *AMP J. Technol.* **5** 37–48
- [4] Irwin G R 1952 Studies in large plastic flow and fracture: with special emphasis on the effects of hydrostatic pressure. P. W. Bridgman. New York-London: McGraw-Hill, 1952. 362 pp. \$8.00 *Science* **115** 424
- [5] Choung J M and Cho S R 2008 Study on true stress correction from tensile tests *J. Mech. Sci. Technol.* **22** 1039–51
- [6] La Rosa G, Mirone G and Risitano A 2001 Effect of stress triaxiality corrected plastic flow on ductile damage evolution in the framework of continuum damage mechanics *Eng. Fract. Mech.* **68** 417–34
- [7] Rosa L, Mirone G and Risitano A 2003 Postnecking elastoplastic characterization: degree of approximation in

- the bridgman method and properties of the flow-stress/true-stress ratio *Metall. Mater. Trans. A* **34** 615–24
- [8] Joun M, Choi I, Eom J and Lee M 2007 Finite element analysis of tensile testing with emphasis on necking *Comput. Mater. Sci.* **41** 63–9
- [9] Joun M, Eom J G and Lee M C 2008 A new method for acquiring true stress–strain curves over a large range of strains using a tensile test and finite element method *Mech. Mater.* **40** 586–93
- [10] Mirone G 2004 A new model for the elastoplastic characterization and the stress–strain determination on the necking section of a tensile specimen *Int. J. Solids Struct.* **41** 3545–64
- [11] Kamaya M 2014 Stress–strain curve estimation procedures for stainless steels based on yield and ultimate strengths *Eng. Fract. Mech.* **127** 194–210
- [12] Majzoubi G H, Fariba F, Pipelzadeh M K and Hardy S J 2015 A new approach for the correction of stress–strain curves after necking in metals *J. Strain Anal. Eng. Des.* **50** 125–37
- [13] Pan B 2018 Digital image correlation for surface deformation measurement: historical developments, recent advances and future goals *Meas. Sci. Technol.* **29** aac55b
- [14] Chu T C, Ranson W F and Sutton M A 1985 Applications of digital-image-correlation techniques to experimental mechanics *Exp. Mech.* **25** 232–44
- [15] Ben David O et al 2014 Evaluation of the mechanical properties of PMMA reinforced with carbon nanotubes—experiments and modeling *Exp. Mech.* **54** 175–86
- [16] Min J, Stoughton T B, Carsley J E and Lin J 2017 A method of detecting the onset of localized necking based on surface geometry measurements *Exp. Mech.* **57** 521–35
- [17] Zhu F, Bai P, Zhang J, Lei D and He X 2015 Measurement of true stress–strain curves and evolution of plastic zone of low carbon steel under uniaxial tension using digital image correlation *Opt. Lasers Eng.* **65** 81–8
- [18] Dumoulin S, Tabourot L, Chappuis C, Vacher P and Arrieux R 2003 Determination of the equivalent stress–equivalent strain relationship of a copper sample under tensile loading *J. Mater. Process. Technol.* **133** 79–83
- [19] Kamaya M and Kawakubo M 2011 A procedure for determining the true stress–strain curve over a large range of strains using digital image correlation and finite element analysis *Mech. Mater.* **43** 243–53
- [20] Yu J H, McWilliams B A and Kaste R P 2016 Digital image correlation analysis and numerical simulation of aluminum alloys under quasi-static tension after necking using the Bridgman’s correction method *Exp. Tech.* **40** 1359–67
- [21] Peirs J, Verleysen P, Van Paeppegem W and Degrieck J 2011 Determining the stress–strain behaviour at large strains from high strain rate tensile and shear experiments *Int. J. Impact Eng.* **38** 406–15
- [22] Besnard G, Hild F, Lagrange J-M, Martinuzzi P and Roux S 2012 Analysis of necking in high speed experiments by stereocorrelation *Int. J. Impact Eng.* **49** 179–91
- [23] Felipe-Sesé L, Siegmann P, Díaz F A and Patterson E A 2014 Simultaneous in-and-out-of-plane displacement measurements using fringe projection and digital image correlation *Opt. Lasers Eng.* **52** 66–74
- [24] Felipe-Sesé L, Siegmann P, Díaz F A and Patterson E A 2014 Integrating fringe projection and digital image correlation for high-quality measurements of shape changes *Opt. Eng.* **53** 044106
- [25] Siegmann P, Felipe-Sese L and Diaz-Garrido F 2017 Improved 3D displacement measurements method and calibration of a combined fringe projection and 2D-DIC system *Opt. Lasers Eng.* **88** 255–64
- [26] Justin Blaber, Ncorr v.1.2 (www.ncorr.com/)
- [27] Dennis J E and Schnabel R B 1996 *Numerical Methods for Unconstrained Optimization and Nonlinear Equations* (Philadelphia, PA: SIAM) (<https://doi.org/10.1137/1.9781611971200>)